Accepted Manuscript

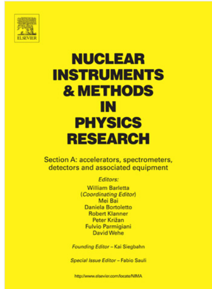

Modeling charge transport in photon-counting detectors

Yuan Fang, Cheng Xu, Yuan Yao, Norbert Pelc, Mats Danielsson, Aldo Badano

PII: S0168-9002(18)30627-2
DOI: https://doi.org/10.1016/j.nima.2018.05.027
Reference: NIMA 60811

To appear in: *Nuclear Inst. and Methods in Physics Research, A*

Received date : 10 June 2017
Accepted date : 12 May 2018

Modeling charge transport in photon-counting detectors

Yuan Fang[a], Cheng Xu[b], Yuan Yao[c], Norbert Pelc[d], Mats Danielsson[b], Aldo Badano[e]

[a]*Division of Radiological Health, Office of In Vitro Diagnostics and Radiological Health, Center for Devices and Radiological Health, Food and Drug Administration, 10903 New Hampshire Ave, Silver Spring, MD 20993 USA.*
[b]*Department of Physics, Royal Institute of Technology, Stockholm, Sweden.*
[c]*Department of Bioengineering, Stanford University, Stanford, California; Department of Radiology, Stanford University, Stanford, California 94305.*
[d]*Department of Bioengineering, Stanford University, Stanford, California; Department of Radiology, Stanford University, Stanford, California; Department of Electrical Engineering, Stanford University, Stanford, California.*
[e]*Division of Imaging, Diagnostics, and Software Reliability, Office of Science and Engineering Laboratories, Center for Devices and Radiological Health, Food and Drug Administration, 10903 New Hampshire Ave, Silver Spring, MD 20993 USA.*

Abstract

The purpose of this study is to review and compare simulation methods for describing the transport of charge clouds in silicon based semiconductor detectors and investigate the effects on energy spectrum for silicon based photon-counting strip detectors. Charge clouds and detailed carrier transport are simulated and compared using two different approaches including analytical and Monte Carlo schema. The results of the simulations are evaluated using pulse-height spectra (PHS) for a silicon strip detector with edge on geometry at two energies (25 and 75 keV) at various x-ray absorption locations relative to the pixel boundary and detector depth. The findings confirm carrier diffusion plays a large role in the charge sharing effect in photon counting detectors, in particular when the photon is absorbed near the pixel boundary far away from the pixel electrode. The results are further compared in terms of the double-counting probability for x-ray photons absorbed near the pixel boundary as a function of the threshold energy. Monte Carlo and analytical models show reasonable agreement (2% relative error in swank factor) for charge sharing effects for a silicon strip detector with edge-on geometry. For 25 keV mono-energetic photons absorbed at 5 μm from the pixel boundary, the theoretical threshold energy at 10% double-counting probability based on charge sharing is 5.5, 8.5 and 9.2 keV for absorption depths of 50, 250 and 450 μm from the electrode, respectively. The transport of charge clouds affects the spectral characteristics of photon counting detectors and the double-counting probability results show the theoretical threshold energy to avoid double-counting as a function of x-ray energy and x-ray interaction locations for silicon and can be considered for future studies of charge sharing effects.

Keywords:
photon-counting, silicon detector, charge-sharing, double-counting probability, Monte Carlo

---

1. Introduction

Photon-counting detectors with energy discrimination capabilities have been recently developed for many medical x-ray imaging applications[1, 2] promising several advances including the ability to estimate the energy of transmitted photons at each pixel location. This technological development could enable improved material decomposition, higher spatial resolution, and implementation of beam hardening corrections.In most cases, photon counting detectors with energy discrimination can achieve higher signal-to-noise ratio[3] leading to improvements in existing modalities or allowing novel applications.[1, 4–8] In addition, photon-counting detectors can be used in spectral CT applications.[9–15]

One major challenge for photon-counting detectors is a phenomenon generally known as charge sharing. Under an externally applied bias, a cloud of charge carriers created by the energy imparted by an absorbed x-ray photon travels within the semiconductor and reaches the detector electrode. Near a pixel boundary, the cloud may be divided and detected simultaneously by multiple pixels recording energies lower than the energy carried by the x-ray quantum. The distribution of energy causes distortions in the spectral response. The significance of this effect depend on the detection material, charge carrier mobility, pixel size, absorption location with respect to the pixel boundary, depth of interaction within the active detector layer, temperature, applied bias (including non-uniform electric field affects due to Frisch grid structures).

Different models have been proposed to simulate charge-sharing effects. Analytical models vary in complexity due to compromises made towards computational simplicity and/or practical solution of the theoretical electrostatic equations. Barrett *et al.* [16] derived a one-dimensional solution to the transport of charge clouds in semiconductor detectors with 2D anode arrays and described how to compute the pulse-height spectra. Rossi[17] adopted a one-dimensional Gaussian model and provided a simple solution in determining the charge split in a microstrip detector. In this model, thermal diffusion was the sole deterministic factor to the spread of the Gaussian profile and the charge loss was ignored. Kozorezov *et al.*[18] developed a drift-diffusion model for computing the collected electron charges as the product of two error functions for the limited trapping case. The solution of the general drift-diffusion model was obtained by factorizing the carrier motion into two separate components, the first describing a purely diffusive process in the lateral direction and the second a mixture of drift and random walk along the normal z direction. This model was generally applicable to the pixelated photon-counting detectors and is material independent. Later on, an extension by Engel *et al.*[19] described the additional contribution from detector polarization in a pixelated x-ray semiconductor detector containing an inhomogeneous electric field parallel to the depth axis caused by different concentration of ionized dopants. X-ray energy deposition and charge movements within the detector were modeled in Monte Carlo simulations giving access to statistical analysis of electron drift time and current pulse widths for various degrees of static polarization.

While analytical models can describe initial trends and be applicable to simplified geometries, Monte Carlo techniques provide an accurate and more flexible method to simulate the response of photon-counting semiconductor detectors for a variety of geometries and system configurations. The interaction and transport mechanisms for x-ray photons in the detector and the generation of secondary particles can be tracked in detail until energy is either transformed into secondaries (electron-hole pairs) or lost out of the detector volume through a radiative process. The mechanisms of photon and electron interaction and transport in semiconductors are complex and can be modeled with existing available codes, e.g. PENELOPE,[20, 21] GEANT4,[22] MCNP,[23] or EGSnrc,[24]. Recently, a comprehensive (spatial and temporal) MC simulation tool, ARTEMIS,[25, 26] for the simulation of photon and secondary electron interactions with the addition of electron-hole pair charged-carrier transport in the presence of a bias electric field became publicly available.

In addition, other numerical techniques including finite element methods (FEM) can be utilized for solving the transport problem in a wide range of semiconductor devices.[27, 28] Based on classical electrodynamics, the electric potential in the detector is computed numerically by solving the Poisson equation with properly set boundary conditions. The existence of surface charge below the oxide layer in the region between electrodes affects the distribution of electric potential. Advanced finite element analysis (FEA) programs can in this case be used to model the charged carrier behavior. FEM and MC methods can also be combined to solve carrier transport problems.[29, 30] In particular, the PENELOPE package has been successfully combined with COMSOL to model charge induction by carriers in photon-counting detectors.[31] In general, numerical techniques using analytical (or semi-analytical) models less calculation time compared to MC techniques. However, they suffer from numerically instability, uncertain appropriate boundary conditions for obtaining meaningful results, and lack of stochastic models necessary for modeling radiation absorption and transport in semiconductor materials.

With many MC and analytical approaches available for modeling radiation transport in semiconductor materials, this work provides a comparison of two models for transport of charged carriers. We study the effect of charge sharing due to the transport of charged carriers in photon-counting silicon detectors as a function of x-ray energy, absorption depth, and absorption location with respect to the pixel boundary with two different models for simulating x-ray and charge carriers in semiconductor materials.[25, 32] Specifically, both analytical[32] and MC[25] models are studied for the charged carrier transport.

2. Methods

In this section, we present the details of the models used in this study for modeling charge sharing effects in photon-counting imaging detectors and describe the computational experiments used to compare the results obtained with the different approaches. The bubble-line and ARTEMIS models utilize MC methods for simulation of photon and electron interactions. The difference between the two models arise from the simulation of transport of charged carriers which is analytical in the bubble-line model.

2.1. Analytical

The production and distribution of initially-released electron-hole pairs, i.e. initial charge cloud, is the first step of the simulation of charge cloud transport. Although a detailed Monte Carlo simulation is preferable, simulations can be time-consuming especially for higher energy photons. Instead, some simplified models are commonly used assuming the initial charge cloud as a sphere with charge inside following either a uniform or Gaussian distribution.[33, 34]

The spherical approximation of initial charge clouds, which is also the basis of analytical approaches, is not capable of modeling the detector response accurately for high-energy photons in medical x-ray imaging energy range. Recently, a statistical model has been proposed to simulate the shape of initial charge clouds by using pre-computed statistical distributions based on Monte Carlo simulation data with promising results.[32]

For the so-called bubble-line model, the initial charge cloud produced by a photon interaction is represented through three pre-extracted parameters: the magnitude and polar angle of the center-of-gravity (COG) vector of the initial charge distribution, and the track size. For a certain photon-deposited energy, the above parameters can be sampled from the corresponding pre-computed probability distributions (two Gaussian distributions and one Weibull distribution), and the parameters of each distribution are simply the results of quadratic functions with the deposition energy as variable and the coefficients known. It is named as bubble-line model because a certain amount of the deposited energy is distributed into a bubble located at the COG and the left energy along a line through the COG. By sampling the COG position and track size statistically based on the pre-simulated MC tracks, the random characteristics of the initial charge distributions are reproduced more accurately than the spherical approximation, and comparable to pure Monte Carlo simulations, with much less simulation time.

After being released, the charge cloud moves towards the corresponding electrodes along the electric field lines and enlarged during the charge-collection process. The charge transport include drift and diffusion and generation of signals by Shockley-Ramo theorem.[35, 36]

Field simulation is performed by solving Poisson equations with, for example, Successive Over-Relaxation method (electric field and weighting field) or by more advanced software which can capture the field distribution at Si-SiO2 interface. For some types of semiconductors with low mobility of charge carriers as a result of deep impurities and structural defects, trapping and recombination of charge carriers should be taken into account and modeled accurately to produce the correct detector response. Depending on the initially-released positions, the charge produced by a photon interaction might be collected by more than one pixel (i.e. charge sharing), leading to double counting in photon-counting semiconductor detectors if the shared charge is larger than the minimum threshold in the neighboring pixel.

2.2. Monte Carlo

ARTEMIS (pArticle transport, Recombination, and Trapping in sEMiconductor Imaging Simulations) is an open-source Monte Carlo simulation package for modeling the charge transport process in radiation imaging detectors.[25, 26] ARTEMIS relies on PENELOPE for the simulation of photon and high-energy electron transport coupled with charge transport routines for the spatio-temporal simulation of electron-hole pair transport under an applied bias. The charge transport routines include three-dimensional spatial and temporal models of electron-hole pair transport taking into account recombination and trapping. Many electron-hole pairs are created simultaneously in bursts from energy deposition events. Carrier transport processes include drift due to external field and Coulombic interactions, and diffusion due to Brownian motion.

When a photon interacts within the photoconductor, high-energy electrons are created and moved in a random walk while they deposit energy at random locations. Electron-hole pairs are generated in bursts from the deposition energies, based on the interaction coordinates, the energy of the interacting particle, and the amount of energy deposited. The number of electron-hole pairs created is sampled based on a Poisson distribution, with the mean calculated based on the ionization energy equation developed by Que and Rowlands.[37] The ionization energy also contributes to the initial electron-hole pair separation described by the Knight-Davis Equation,[38] as a function of the amount of energy deposited and applied electric field. Once the electron-hole pairs are initialized in bursts, the electric field pulls the particles toward opposed electrodes and the electrons and holes may get trapped or recombine.[39] Recombination can occur when an electron and a hole travel toward each other, and trapping can occur when an electron or a hole reaches a lower energy state due to material impurities. During transport, carriers are subject to drift from both the applied electric field and Coulomb field due to other charge carriers. Each carrier is also subject to random Brownian diffusion as a function of temperatures and carrier mobility.

The ARTEMIS material properties including carrier mobility reflect those of the simulated detectors. Recombination and trapping are disabled while Coulombic interactions are not considered because, compared to Selenium carrier interactions in silicon such as recombination and trapping from initial charge cloud creation do not lead to significant loss in the detector signal. The electronic noise during readout is not modeled and only electrons are detected.

Material property	**Si**	**a-Se**	**CdZnTe**
Bandgap (eV)	1.1	2.3	1.7
Applied E-field ($V/\mu m$)	0.30	10	0.25
Ionization energy (eV)	3.62	∼5	4.6
Measured Fano factor	0.11	0.059	0.089
Hole mobility, μ_h (cm^2/Vs)	480	0.14	50
Electron mobility, μ_e (cm^2/Vs)	1350	5×10^{-3}	1000
Hole lifetime, $\tau_h(s)$	2×10^{-3}	10^{-6}	10^{-6}
Electron lifetime, $\tau_e(s)$	10^{-3}	10^{-6}	3×10^{-6}

Table 1. Material and transport properties of semiconductor materials.[37, 40–44]

These modifications have led to significant speed-ups in the simulation by at least ten times depending on the simulation conditions. Table 1 lists the material properties and transport parameters for different semiconductor materials including Si, a-Se and CdZnTe. All models in this study use the same set of simulation parameters and edge on geometry described in Figure 1.

A comparison of the bubble-line and ARTEMIS models for x-ray and electron transport, charge cloud creation and carrier transport models can be found in Table 2.

2.3. Detector Simulation Geometry

Figure 1 illustrates the silicon strip detector geometry and set up used in this study. Specifically, the pixel size is 50 μm wide, with a strip length of 1 *cm* and a thickness of 500 μm. We simulated 9 x-ray absorption locations to cover a range relative to the inter-pixel boundary and electrodes. This includes 3 incident x-ray locations 5, 15 and 25 μm away from the pixel boundary and 3 x-ray absorption depths, 50, 250 and 450 μm from the pixel electrode. This configuration is applicable to all the models in order to provide a basis for fair comparison of the simulation results.

2.4. Double-counting

The double-counting probability ($DC_{probability}$) of a carrier being absorbed in a secondary pixel is defined as the product of probability of absorption in the

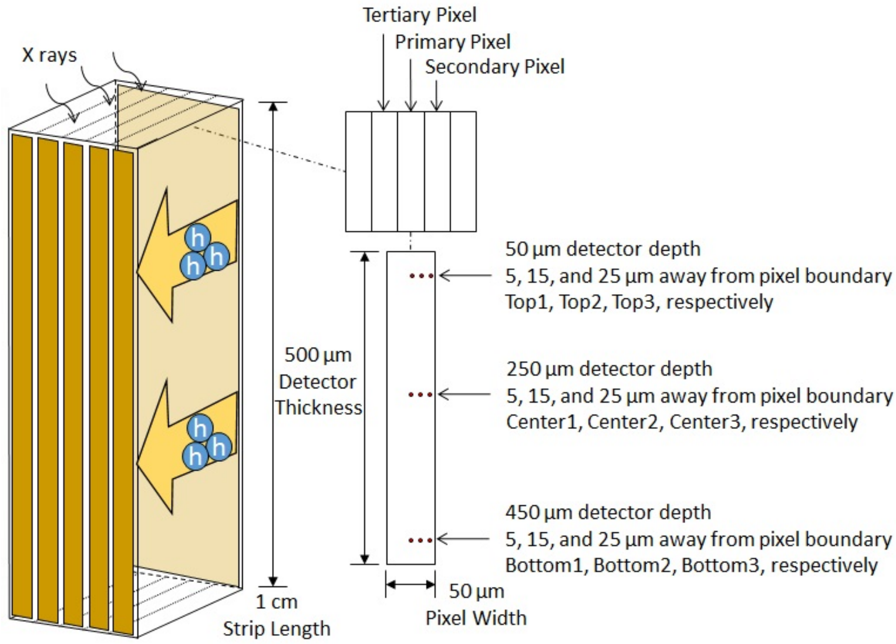

Figure 1. Silicon strip detector used for simulation purposes. The edge-on geometry has x rays incident from the top and electrodes on the side. Large arrows within the strip detector indicate the direction of carrier motion for holes. The pixel size is 50 μm, and the incident x ray location are 5, 15 and 25 μm from the pixel boundary. The detector thickness is 500 μm, and the absorption depth are 50, 250 and 450 μm from the pixel electrode.

Model	X-ray and electron transport	Cloud creation model	Charge transport model
Bubble-line[32]	PENELOPE[20]	All energy deposited in the semiconductor material is uniformly distributed in a sphere at center-of-gravity of the electron track and along a line through COB	Carrier drift, Brownian diffusion, holes only (electrons are not considered).
ARTEMIS[25]	PENELOPE[20]	The electrons are simulated and tracked individually with energy deposited at site of each electron interaction	Carrier drift, Brownian diffusion, electrons only (holes are not considered). Disabled features include Coulombic interactions, recombination of electron-hole pairs, carrier trapping and electronic noise.)

Table 2. Models used in this paper to compare charge-sharing effects.

primary (p_p) and secondary (p_s) pixels shown below as a function of threshold energy (E_t):

$$DC_{probability}(E_t) = p_p(E_t)p_s(E_t) \ , \tag{1}$$

where the probability of count in the pixel i is defined as the pulse-height spectrum ($\mathcal{P}$) integrated and then divided by the threshold energy and photon energy (E_p) over the entire count of $\mathcal{P}$.

$$p_i(E_t) = \frac{\int_{E_t}^{E_p} \mathcal{P}_i(E)dE}{\int_0^{E_p} \mathcal{P}_i(E)dE} \ . \tag{2}$$

The secondary and tertiary pixels are the two neighboring pixels next the the primary pixel where the x-ray photon is absorbed shown in Fig. 1. When the x-ray photon is absorbed near the pixel boundary, not in the pixel center, the secondary pixel is defined as the pixel closer the x-ray interactions site, and the tertiary is the pixel on the opposite side further away from the x-ray interaction location. In this definition, the double-counting probability is a value between 0 and 1. In addition, the double-counting probability is only for the charge sharing effects and not take into account timing information such as pile-up in the detector.

An alternative metric can be defined as the double counting percentage ($DC_{percentage}$) as a ratio of collected charges[45]:

$$DC_{percentage}(E_t) = \frac{(C_s + C_t)}{C_p} \ , \tag{3}$$

where the amount of charge collected in the primary (C_p), secondary (C_s) and tertiary (C_t) pixels are considered.

3. Results

3.1. Pulse-height spectra

Pulse-height simulation results for 25 keV mono-energetic x-ray photons are presented in Figure 2. The x-axis is the number of holes collected from each interacted x-ray photon and the y-axis is the number of primary x-ray absorption events normalized to peak of unity. For the 25 keV case where the incident x-ray is absorbed very close (5 μm) to the pixel boundary and 50 μm from the pixel electrode, $\mathcal{P}$ contains a spectral tail due the diffusion of charge carriers. $\mathcal{P}$ further degrades in terms of total count of carriers detected and the spectral width increases as the absorption depth increases from the pixel electrode (250 and 450 μm). This is due to the more significant diffusion effects as a result of the increase in the distance the charge carrier must travel to reach the pixel electrode and due to the random walk by the high-energy electron leading to a charge cloud of electron-hole pairs created. As the incident x-ray photon interaction location moves further away (15 and 25 μm) from the pixel boundary, $\mathcal{P}$ recovers and the effects of charge carrier transport become less pronounced.

The bubble-line and ARTEMIS models show good agreement in the simulation results. This is because semiconductor detectors such as silicon have much higher carrier mobility and lifetime compared to Se-based detectors as shown in Table 1, resulting in negligible trapping and recombination rates. In these types of materials, charge sharing is mainly due to carrier diffusion affected by the x-ray photon absorption location near the pixel boundary and distance to the electrode. That said, there are some differences in $\mathcal{P}$, especially for cases

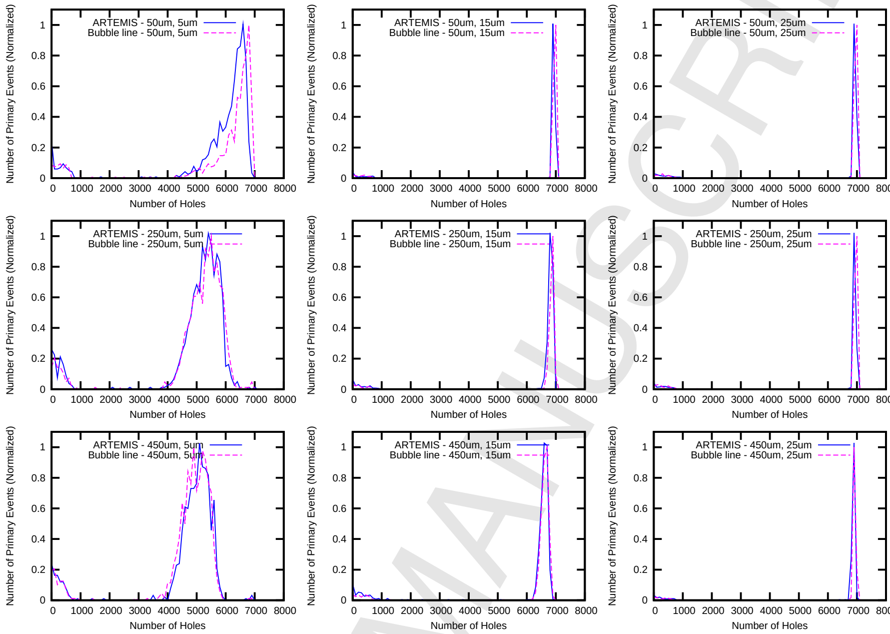

Figure 2. Pulse-height simulation results for 25 keV mono-energetic x-ray photon with bubble-line and ARTEMIS models including a wide range of x-ray absorption locations and pixel boundaries.

where the photon is absorbed near the pixel boundary which can be attributed to statistical MC noise.

For the 75 keV case shown in Figure 3, similar trends are observed in $\mathcal{P}$ as a function of x-ray interaction location from pixel boundary and absorption depth in the detector. The main difference between the 25 and 75 keV cases is the increase of counts at lower energies due to Compton scattering.

3.2. Double-counting

Figure 4 (a) and (b) show the probability of a signal is counted in the primary, secondary and tertiary pixels as a function of threshold energy. For both 25 and 75 keV cases, the probability of count in the tertiary pixel is very low and is not considered in the double-counting probability calculations in this work. In addition, the double-counting probability is only for the charge sharing effects

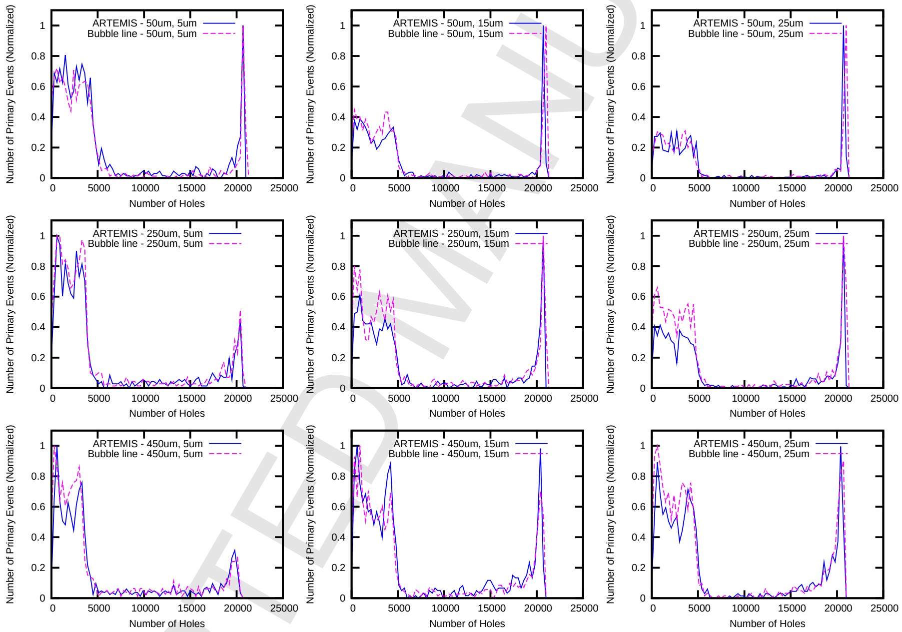

Figure 3. Pulse-height simulation results for 75 keV mono-energetic x-ray photons with bubble-line and ARTEMIS models including a wide range of x-ray absorption locations and pixel boundaries.

and not take into account timing information such as pile-up in the detector.

The double-counting probability is calculated based on the ARTEMIS $\mathcal{P}$ simulation results are shown in Figure 4 (c) and (d). The double-counting probability is highest for the case where the x-ray interaction is closest to the pixel boundary (5 μm) and farthest from the pixel electrode (450 μm) and slowly decreases when the absorption depth is closer to the pixel electrode. This is consistent with the results for $\mathcal{P}$, where $\mathcal{P}$ improves as the absorption depth from pixel electrode is reduced. For the 25keV case with x-ray interaction 5 μm from the pixel boundary, the threshold energy at 10% double-counting probability is 5.5, 8.5 and 9.2 keV for absorption depth 50, 250 and 450 μm from electrode, respectively. This calculated is for mono-energetic x-ray photons, and considers primary and secondary pixels. However, based on a 50 μm pixel width, the effect of tertiary and higher order pixels is very small, as shown by the probability of interaction based on threshold energy plots in Figure 4. Therefore, depending on the depth in the detector where the photons are absorbed, the double-counting probability varies.

In addition, double counting is also evaluated using Equation 3. The double-counting percentage for 25 keV mono-energetic photons is shown in Figure 5 with the same conditions as in Figure 4 (c). For various photon absorption depths (50, 250 and 450 μm) the double-counting percentage and probability results exhibit similar trends as a function of threshold energy.

4. Discussion

We compared the bubble-line and ARTEMIS models for the characterization of charge-sharing effects in semiconductor x-ray detectors. The simulated PHS results shows good agreement when no trapping and recombination are used. This comparison is based on the relative error in Swank factor[46, 47] calculated based on the PHS. The models attribute charge sharing mainly to carrier diffusion affected by the x-ray photon absorption location near the pixel boundary and distance to the electrode. This result is applicable to semiconductor mate-

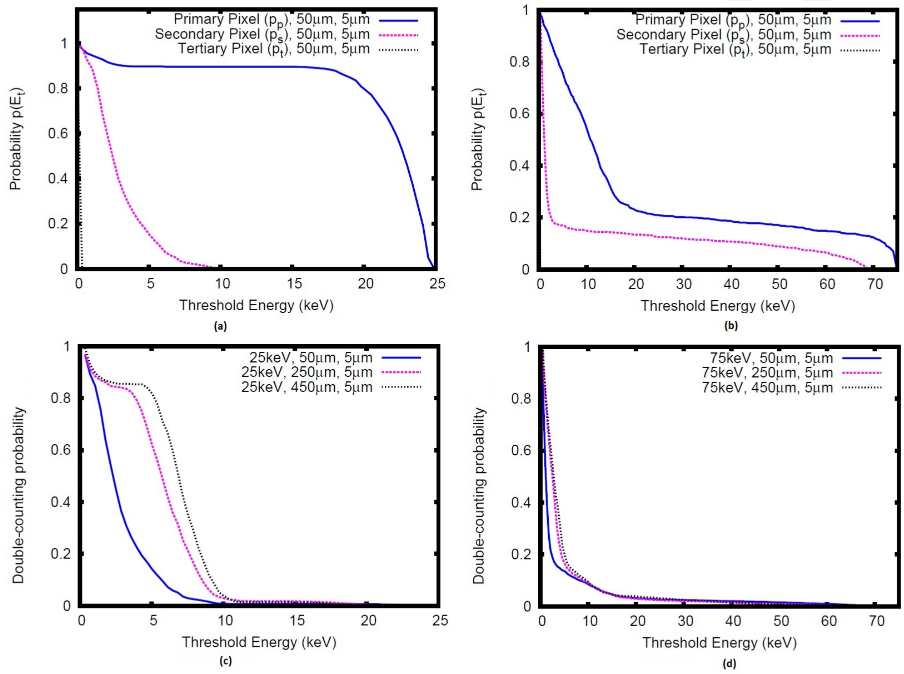

Figure 4. Simulated double-counting probability results: (a) Probability of a signal being counted in the primary, secondary and tertiary pixels as a function of threshold energy for 25 keV mono-energetic photons. (b) The probability a signal is counted in the primary, secondary and tertiary pixels as a function of threshold energy for 75 keV mono-energetic photons. Double-counting probability results for (c) 25 keV mono-energetic photons, and (d) for 75 keV mono-energetic photons.

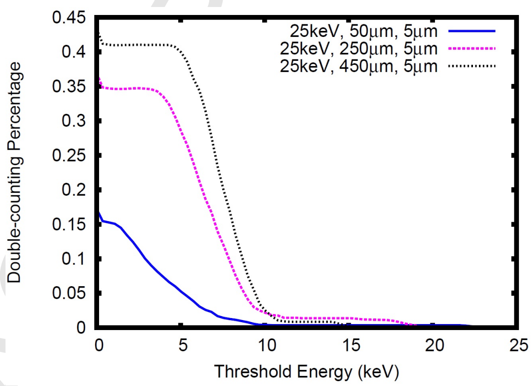

Figure 5. Double-counting percentage results for 25 keV mono-energetic photons.

rials such as silicon with high carrier mobility and lifetime but might not apply to relatively higher density materials such as Se and CdZnTe. A speed up of more than 10 times was observed for the ARTEMIS model simulation times by not taking into account recombination and trapping.

The effect of charge sharing depends strongly on the location of x-ray absorption near the pixel boundary. In this study, three absorption locations were used. The case at 25 μm from the pixel boundary is at the pixel center with 50 μm pixel width. The closest photon absorption location to the pixel boundary is 5 μm. In future work, more absorption locations could be studied to fully describe the charge-sharing effect. In addition, we used mono-energetic x-ray photons to minimize Swank noise from a polychromatic spectrum. In order to study charge-sharing effects in clinical x-ray systems, clinical spectral x-ray distributions should be used. At any rate, the study of double-counting probability can be used to understand the fundamental energy threshold limitations for system design in photon counting applications including the use of multiple energy thresholds for novel imaging applications.

For double-counting, we used two different metrics that are calculated using the charge transport simulation results described in this paper. The probability definition of double-counting depends on the probability of count in specific pixels (primary, secondary, tertiary, etc) and is a value between 0 and 1. This definition can be used to isolate the double-counting probability in individual pixels and normalized to 1 independently of pixel size. The percentage metric is based on the amount of charge collected and is a ratio between counts in the primary and neighbouring pixels, and can be greater than 1 for small pixels.

Overall, the comparison of models described in this paper has the following limitations. First, in ARTEMIS, recombination and trapping effects were disabled to provide a direct comparison with the bubble-line method. Since carrier mobility is high in silicon compared to a-Se, recombination and trapping were assumed to be negligible. However, for other types of materials, these effects may be significant and can be included in future work. Table 1 lists the material properties for Si, a-Se and CdZnTe. Finally, the detection geometry can play a significant role in charge sharing. In particular, the results obtained for the edge on geometry used in this study for silicon detectors might be different from results obtained for other detection materials with vertical geometry as seen in spectral CT systems being developed.[6, 7]

5. Conclusion

Charge clouds and their transport affect the spectral characteristics of photon counting detectors. These effects are most pronounced when interactions occur near pixel boundaries and can be simulated with Monte Carlo and analytical tools. Results of the model comparison show reasonable agreement for the pulse-height spectra simulations (2% relative error in Swank factor) between the bubble-line and ARTEMIS models when considering a silicon strip detector with two mono-energetic beams (25 and 75 keV). The comparison results indicate that carrier diffusion plays a large role in photon-counting detectors, particularly when the photon is absorbed near the pixel boundary far away from the pixel electrode. In addition, the double-counting probability and percentage for x-ray photons absorbed near the pixel boundary as a function of the threshold energy has been simulated. This work contributes to our understanding of modeling efforts designed to guide future studies of charge-sharing effects in different detection materials, detector arrangements, absorption locations and at different levels of x-ray energy thresholds.

Acknowledgments

The mention of commercial products herein is not to be construed as either an actual or implied endorsement of such products by the Department of Health and Human Services. This is a contribution of the FDA and is not subject to copyright.

References

[1] K. Taguchi, J. S. Iwanczyk, Vision 20/20: Single photon counting x-ray detectors in medical imaging, Medical Physics 40 (10) (2013) 100901.

[2] E. Fredenberg, M. Hemmendorff, B. Cederstrom, M. Aslund, M. Danielsson, Contrast-enhanced spectral mammography with a photon-counting detector, Medical Physics 37 (5) (2010) 2017–2029.

[3] M. Overdick, C. Baumer, K.J. Engel, J. Fink, C. Hermann, H. Kruger, M. Simon, R. Steadman, and G. Zeitler, Towards direct conversion detectors for medical imaging with X-rays, IEEE Nucl. Sci. Conf. R. NSS (2008) 1527.

[4] J.S. Iwanczyk, E. Nygard, O. Meirav, J. Arenson, W.C. Barber, N.E. Hartsough, N. Malakhov, J.C. Wessel, Photon counting energy dispersive detector arrays for x-ray imaging, Nuclear Science, IEEE Transactions on 56 (3) (2009) 535–542.

[5] W.C. Barber, E. Nygard, J.S. Iwanczyk, M. Zhang, E.C. Frey, B.M. Tsui, J.C. Wessel, N. Malakhov, G. Wawrzyniak, N.E. Hartsough, T. Gandhi, Characterization of a novel photon counting detector for clinical CT: count rate, energy resolution, and noise performance, SPIE Medical Imaging, International Society for Optics and Photonics (2009) 725824.

[6] S. Kappler, F. Glasser, S. Janssen, E. Kraft, and M. Reinwand, A research prototype system for quantum-counting clinical CT, SPIE Medical Imaging. International Society for Optics and Photonics (2010) 76221Z.

[7] S. Kappler, T. Hannemann, E. Kraft, B. Kreisler, D. Niederloehner, K. Stierstorfer, T. Flohr, First results from a hybrid prototype CT scanner for exploring benefits of quantum-counting in clinical CT, SPIE Medical Imaging. International Society for Optics and Photonics (2012) 83130X.

[8] R.J., Acciavatti, and A.D. Maidment, A comparative analysis of OTF, NPS, and DQE in energy integrating and photon counting digital x-ray detectors, Medical Physics 37 (12) (2010) 6480–6495.

[9] H. Chen, B. Cederstr$\ddot{o}$m, C. Xu, M. Persson, S. Karlsson, M. Danielsson, A photon-counting silicon-strip detector for digital mammography with an ultrafast 0.18-μm CMOS ASIC, Nuclear Instruments and Methods in Physics Research Section A: Accelerators, Spectrometers, Detectors and Associated Equipment 749 (0) (2014) 1–6.

[10] H. Bornefalk, M. Danielsson, Photon-counting spectral computed tomography using silicon strip detectors: a feasibility study, Phys. Med. Biol. 55 (2010) 1999–2022.

[11] M. Persson, B. Huber, S. Karlsson, X. Liu, H. Chen, C. Xu, M. Yveborg, H. Bornefalk and M. Danielsson, Energy-resolved ct imaging with a photon-counting silicon-strip detector, Phys. Med. Biol. 59 (2014) 6709–6727.

[12] E. Roessl and R. Proksa, K-edge imaging in x-ray computed tomography using multi-bin photon-counting detectors, Phys. Med. Biol. 52 (2007) 4679.

[13] J.P. Ronaldson, R. Zinon, N.J.A. Scott, S.P. Gieseg, A.P. Butler, P.H. Butler, and N.G. Anderson, Toward quantifying the composition of soft tissues by spectral ct with medipix3, Med. Phys. 39 (2012) 6847–6857.

[14] J. Schlomka, E. Roessl, R. Dorscheid, S. Dill, G. Martens, T. Istel, C. Bäumer, C. Herrmann, R. Steadman, G. Zeitler and A. Livne, Experimentally feasibility of multi-energy photon-counting k-edge imaging in pre-clinical computed tomography, Phys. Med. Biol. 53 (2008) 4031.

[15] P.M. Shikhaliev, Energy-resolved computed tomography: first experimental results, Phys. Med. Biol. 53 (2008) 5595.

[16] H. H. Barrett, J. D. Eskin, H. B. Barber, Charge transport in arrays of semiconductor gamma-ray detectors, Phys. Rev. Lett. 75 (1995) 156–159.

[17] G. Rossi, M. S. del Rio, P. Fajardo, J. Morse, Monte Carlo simulation of the x-ray response of a germanium microstrip detector with energy and position resolution, Nuclear Instruments and Methods in Physics Research Section A: Accelerators, Spectrometers, Detectors and Associated Equipment 432 (1) (1999) 130 – 137.

[18] A. G. Kozorezov, J. K. Wigmore, A. Owens, R. den Hartog, A. Peacock, Analytic model for the spatial and spectral resolution of pixellated semiconducting detectors of high-energy photons, Journal of Applied Physics 97 (7) (2005) 074502.

[19] K. J. Engel, C. Herrmann, Simulation of one-dimensionally polarized x-ray semiconductor detectors, Proc. SPIE 7961 (2011) 79610W–79610W–12.

[20] F. Salvat, J. M. Fernández-Varea, J. Sempau, PENELOPE-2006: A code system for Monte Carlo simulation of electron and photon transport, in: Workshop Proceedings, 2006.

[21] J. Baro, J. Sempau, J. Fernández-Varea, F. Salvat, PENELOPE: an algorithm for Monte Carlo simulation of the penetration and energy loss of electrons and positrons in matter, Nuclear Instruments and Methods in Physics Research Section B: Beam Interactions with Materials and Atoms 100 (1) (1995) 31–46.

[22] S. Agostinelli, J. Allison, K. a. Amako, J. Apostolakis, H. Araujo, P. Arce, M. Asai, D. Axen, S. Banerjee, G. Barrand, et al., GEANT4–a simulation toolkit, Nuclear instruments and methods in physics research section A: Accelerators, Spectrometers, Detectors and Associated Equipment 506 (3) (2003) 250–303.

[23] F. B. Brown, et al., MCNP–a general Monte Carlo N-particle transport code, version 5, Los Alamos, NM: Los Alamos National Laboratory.

[24] I. Kawrakow, D. Rogers, The EGSnrc code system: Monte Carlo simulation

of electron and photon transport Technical Report PIRS-701, (Ottawa, Canada: National Research Council of Canada).

[25] Y. Fang, A. Badal, N. Allec, K. S. Karim, A. Badano, Spatiotemporal Monte Carlo transport methods in x-ray semiconductor detectors: application to pulse-height spectroscopy in a-Se., Med Phys 39 (1) (2012) 308–319.

[26] Y. Fang, K. S. Karim, A. Badano, Effect of burst and recombination models for Monte Carlo transport of interacting carriers in a-Se x-ray detectors on Swank noise, Medical Physics 41 (1) (2014) 011904.

[27] COMSOL Multiphysics 4.2a release note (2011).

[28] SYNOPSYS TCAD, SENTAURUS Device: Versatile, multifunctional device simuulator, datasheet (2007).

[29] S. Babiker, A. Asenov, J. R. Barker, and S. P. Beaumont, Finite element Monte Carlo simulation of recess gate compound FFTs, Solid-State Electron. 39 (1995) 629.

[30] T. Hayashi, Y. Kashio, and E. Okada, Hybrid Monte Carlo-diffusion method for light propagation in tissue with a low-scattering region, Appl. Opt. 42 (2003) 2888.

[31] A. Makeev, M. Clajus, S. Snyder, X. Wang, S.J. Glick, Evaluation of position-estimation methods applied to CZT-based photon-counting detectors for dedicated breast CT, Journal of Medical Imaging 2 (2) (2015) 023501.

[32] C. Xu, M. Danielsson, H. Bornefalk, Validity of spherical approximations of initial charge cloud shape in silicon detectors, Nuclear Instruments and Methods in Physics Research Section A: Accelerators, Spectrometers, Detectors and Associated Equipment 648 (2011) S190–S193.

[33] L.K. Townsley, P.S. Broos, G. Chartas, E. Moskalenko, J.A. Nousek, G.G. Pavlov, Simulating CCDs for the chandra advanced ccd imaging spectrometer, Nuclear Instruments and Methods in Physics Research Section A:

Accelerators, Spectrometers, Detectors and Associated Equipment 486(3) (2002) 716.

[34] B. G. Lowe, An analytical description of low-energy X-ray spectra in Si (Li) and HPGe detectors., Nuclear Instruments and Methods in Physics Research Section A: Accelerators, Spectrometers, Detectors and Associated Equipment 439(2) (2000) 247.

[35] W. Shockley, Currents to conductors induced by a moving point charge, J. Appl. Phys. 9 (1938) 635.

[36] S. Ramo, Currents induced by electron motion, proc. IRE 27 (9) (1939) 584.

[37] W. Que, J. Rowlands, X-ray photogeneration in amorphous selenium: Geminate versus columnar recombination, Phys. Rev. B 51 (1995) 10500–10507.

[38] J. Knight, E. Davis, Photogeneration of charge carrier in amorphous selenium, J. Phys. Chem. Solids 35 (1975) 542–554.

[39] D. Sharma, Y. Fang, F. Zafar, K. Karim, A. Badano, spatio-temporal Monte Carlo transport of interacting carriers in semiconductors, App. Phys. Let. 98 (2011) 242111.

[40] G. Belev, S. Kasap, Amorphous selenium as an x-ray photoconductor, Physics of Non-Crystalline Solids 345-346 (2004) 484.

[41] S. Del Sordo, L. Abbene, E. Caroli, A. M. Mancini, A. Zappettini, P. Ubertini, Progress in the development of cdte and cdznte semiconductor radiation detectors for astrophysical and medical applications, Sensors 9 (2009) 3491.

[42] M. Ruat, G. Potter, M. R. Dimmock, A. Berry, Modeling of high count rate energy resolving cdte pixel detector for the performance characterisation of

a medical imaging system, Nuclear Science Symposium Conference Record (NSS/MIC) (2010) 3765.

[43] R. Redus, J. Pantazis, A. Huber, V. Jordanov, J. Buter, B. Apotovsky, Fano Factor Determination for CZT, MRS Proceedings 487 (1997) 101.

[44] A. Darbandi, E. Devoie, O. Di Matteo, O. Rubel, Modeling the radiation ionization energy and energy resolution of trigonal and amorphous selenium from first principles, J.Phys.: Condens. Matter 24 (2012) 455502.

[45] C. Xu, M. Danielsson, H. Bornefalk, Evaluation of energy loss and charge sharing in cadmium telluride detectors for photon-counting computed tomography, Nuclear Science, IEEE Transactions on 58 (3) (2011) 614–625.

[46] R. Swank, Absorption and noise in x-ray phosphors, J. App. Phys. 44 (1973) 4199.

[47] A. Ginzburg, C. Dick, Image Information transfer properties of x-ray intensifying screens in the energy range from 17 to 320 keV, Med. Phys. 20 (1993) 1013.

FigureCaption

Fig. 1 Silicon strip detector used for simulation purposes. The edge-on geometry has x rays incident from the top and electrodes on the side. Large arrows within the strip detector indicate the direction of carrier motion for holes. The pixel size is 50 μm, and the incident x ray location are 5, 15 and 25 μm from the pixel boundary. The detector thickness is 500 μm, and the absorption depth are 50, 250 and 450 μm from the pixel electrode.

Fig. 2 Pulse-height simulation results for 25 keV mono-energetic x-ray photon with bubble-line and ARTEMIS models including a wide range of x-ray absorption locations and pixel boundaries.

Fig. 3 Pulse-height simulation results for 75 keV mono-energetic x-ray photons with bubble-line and ARTEMIS models including a wide range of x-ray absorption locations and pixel boundaries.

Fig. 4 Simulated double-counting probability results: (a) Probability of a signal being counted in the primary, secondary and tertiary pixels as a function of threshold energy for 25 keV mono-energetic photons. (b) The probability a signal is counted in the primary, secondary and tertiary pixels as a function of threshold energy for 75 keV mono-energetic photons. Double-counting probability results for (c) 25 keV mono-energetic photons, and (d) for 75 keV mono-energetic photons.

Fig. 5 Double-counting percentage results for 25 keV mono-energetic photons.